

# Pure spin pumping in 2d van der Waals heterostructures

---

Master 2 Internship report

**Karen Sobnath**

**Supervisors: François Mallet and Clément Barraud**

Laboratoire Matériaux et Phénomènes Quantiques

Université de Paris

June 15, 2021

# Contents

<b>1</b>	<b>Introduction</b>	<b>2</b>
<b>2</b>	<b>Theoretical background</b>	<b>5</b>
2.1	Ferromagnetism . . . . .	5
2.1.1	Hamiltonian . . . . .	6
2.1.2	Landau-Lifschitz-Gilbert equation . . . . .	6
2.1.3	Ferromagnetic resonance . . . . .	7
2.2	Spintronics of FM/NM bilayers . . . . .	7
2.3	Spin pumping . . . . .	8
2.4	Inverse spin Hall effect . . . . .	9
<b>3</b>	<b>My work</b>	<b>11</b>
3.1	Simulations . . . . .	11
3.2	Optical masks . . . . .	15
3.3	Nanofabrication . . . . .	17
3.4	Measurements . . . . .	21
<b>4</b>	<b>Conclusion</b>	<b>25</b>
	<b>Bibliography</b>	<b>26</b>

# Introduction

The transistor has been invented in 1947 by Bardeen, Brattain, and Shockley [1], who received the Nobel Prize of Physics in 1956. The potential of transistors has been brought to light with the integration of the first Metal-Oxide-Semiconductor Field Effect Transistor (MOSFET) in integrated circuits. It has started and continues to bring unprecedented impacts on the society. This success has been driven by transistor scaling codified by the Moore's law [2]. It states that the number of transistors on a chip is expected to double approximately every 1.5-2 years. Indeed, it has been confirmed by the release of new generations of technologies exactly within this interval of time referred to as technology nodes. Each technology node is characterised by the pitch, i.e. the smallest distance between two metal lines. As the pitch is decreased, the density of transistors on a chip is correspondingly increased. It has allowed either more functionality for a given chip size or has given the possibility to reduce the chip to a given level of functionality. The chip/wafer ratio is largely improved. Nowadays, tens of billions of MOSFETs are packed into commercially available microprocessors. Besides the spatial benefit, lower power consumption and higher clock frequency for advanced logic devices were successfully targeted.

However, the ongoing miniaturization turned out to be challenging starting from the 20 nm node, with Short Channel Effects (SCE) coming into play. The reduction of the voltage supply combined with the reduction of the threshold voltage to satisfy the need for maintaining a high current in the device has led to an exponential increase of the leakage current. Moreover, the transistor was no more reliable because of the total loss of gate control. Therefore, to meet the society requirements on scalability, innovations were necessary in a number of areas including processing technologies, device structures, materials and transport physics [3]. For example, modulation of the doping has been explored such as lightly doped source and drain extensions known as LDD which prevent SCE and threshold voltage roll-off. In the last years, technology solutions acting on the very material composition have been studied. Velocity saturation effects in the channel has brought the idea of straining the channel through the use of embedded stressors inserted into the source and drain regions, producing strain laterally on the channel

[4]. Thus, it led to efficient enhancement of the carrier mobility. Concerning the gate, high  $\kappa$  dielectrics appeared as good candidates to replace  $\text{SiO}_2$  as the gate oxide to minimize tunneling current. More recently, the change of the MOSFET structure has been considered to pursue transistor scaling, bringing to the conception of new devices exploiting 3 dimensions named FinFETs where the gates wraps around a thin-shaped silicon body. It has significantly faster switching times and higher current density than a planar technology [5]. Nevertheless, when scaling the FinFETs even more, the main issues related to SCE still remains.

Since conventional electronics have been facing many obstacles, spintronics has been quickly positioned as an attractive field. It relies on the control and manipulation of the intrinsic angular momentum of electrons: the spin. The discovery of Giant Magneto-Resistance (GMR) in 1988 by Albert Fert [6] and Peter Grünberg [7] has launched active researches on nanomagnetism and spintronics. It has been demonstrated that due to the splitting of the energy bands of spin up and spin down directions, the electrons carrying the electrical current at the Fermi level exhibit different conduction properties. Together with the proof of the existence of antiferromagnetic interlayer exchange coupling in Fe/Cr multilayers, it has been found the possibility to switch the relative magnetization of an adjacent magnetic layer with a magnetic field. Thus, huge efforts have been put into studying these spin valves made of ferromagnetic layers spaced by a nonmagnetic material layer. The resistance through the device relies on the relative alignment of the two ferromagnetic layers: the high resistance state is associated to the anti parallel configuration of the ferromagnetic layers while the low resistance state is associated to the parallel configuration. Therefore, the concept of GMR has been implemented in hard-drive read head, increasing considerably the density of stored information. Nowadays, these conventional hard-drive have been replaced by more sensitive technologies based on Tunnel Magneto-Resistance (TMR). TMR has been discovered by Julliere in 1975 [8]. TMR-based devices consist in a thin insulator layer between two ferromagnetic layers where spin-up electrons can only tunnel into spin-up states and spin-down electrons can only tunnel into spin-down states. As for GMR, the current flowing through the TMR device can be modified by applying a magnetic field.

In parallel to the rise of spintronics, the interest for 2d van der Waals materials has open the way to new opportunities for spintronics owing to their unusual physical properties [9, 10]. For example, graphene has been very popular. It has been proven to be an ideal material for spintronics because it exhibits spin relaxation time on the order of 10 ns and spin relaxation lengths on the order of several tens of  $\mu\text{m}$  [11]. Other 2d van der Waals materials have attracted attention. Hexagonal Boron Nitride (hBN) is used as a dielectric insulator and has been demonstrated to enhance the mobility of graphene and  $\text{MoS}_2$  when encapsulated in hBN. Another promising class of materials is the family of

transition metal dichalcogenides (TMDs) among which  $\text{MoS}_2$  is the most widely studied one [12]. TMDs display a variety of properties such as direct band gap, atomic-scale thickness, strong spin orbit coupling and spin-valley locking, which makes them highly attractive in a broad spectrum of applications, including naturally spintronics. Indeed, the strong spin-orbit coupling paves the way to manipulate spins with only charges [13]. In addition to this broad range of properties, the possibility to stack 2d materials together and form heterostructures has attracted a lot of the attention towards these materials. For example, when two layers of graphene are assembled and twisted by a specific angle, the phase diagram exhibits insulator states as well as superconducting states [14]. Other attractive heterostructures which has been investigated is composed of graphene and  $\text{WSe}_2$  for instance where this stacking becomes a meta-material which inherits the best properties of its two components, namely high mobility due to graphene and strong spin orbit due to the TMDs [15].

During my internship, I worked with the TELEM group in the laboratory Matériaux et phénomènes quantiques who masters the nanofabrication of 2d van der Waals heterostructures. Previous works have already been done regarding this class of materials. For instance, a spin field effect transistor in a TMD,  $\text{WSe}_2$  has been investigated and has reported very encouraging results. In this perspective, the efforts have been pursued towards the characterization of the basic spin transport properties into 2d van der Waals materials to the aim of contributing to the development of spin logic devices. In particular, my work has been focused on a developing a completely new spin injection method for our group, namely spin pumping. Efficient spin injection is the first crucial step in order to implement effective new spintronic devices.

# Theoretical background

## 2.1 Ferromagnetism

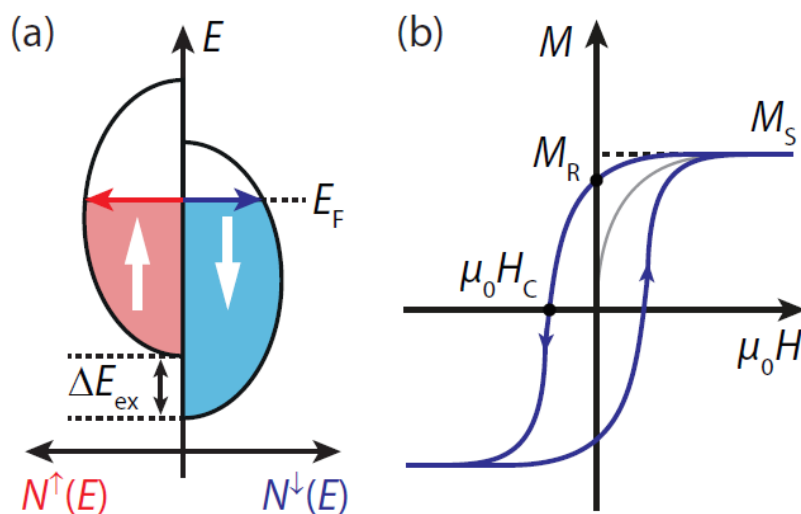


**Figure 2.1:** (a) Density of states of spin-up ( $N_\uparrow$ ) and spin-down ( $N_\downarrow$ ) and (b) magnetization as a function of external magnetic field of a ferromagnetic material.

At the microscopic scale, in ferromagnetic materials, spins spontaneously tend to align. This property gives to the system a non-zero magnetic moment below Curie temperature ( $T_c$ ). The system is considered as a continuous medium where the distribution of the magnetic moment are described by the vector magnetization  $\mathbf{M}$ . When all the magnetic moment are parallel, the material is in ferromagnetic order and the magnetization is said at saturation which is denoted as  $\mathbf{M}_s$ . Originally, the spontaneous ferromagnetic ordering occurs if the Stoner criterion  $I^* \text{Dos}(E_f) > 1$  is satisfied, with  $I$  being the Stoner parameter. A large exchange interaction and a large density of state at the Fermi level is generally required. The characteristic band splitting by the exchange splitting  $\Delta E_{ex}$  is responsible for the spontaneous magnetization  $M_s$  which is proportional to the density of spin-up electrons  $n_\uparrow$  and to the density of spin-down electrons  $n_\downarrow$ , in the absence of

an external magnetic field. When an external magnetic field  $H_{ext}$  is applied parallel to the magnetisation  $\mathbf{M}_s$ , as depicted in figure 2.1, one observes an hysteresis cycle for the magnetisation, which aligns with the direction of the external field  $H$  when its magnitude exceed the coercive field  $\pm H_c$ , the sign depending on the initial magnetization orientation.

### 2.1.1 Hamiltonian

The total energy of a magnetic system is described by its Hamiltonian  $H$ . It can be expressed as a sum of all energies which affect the magnetization of the system. The total energy density can be written as:

$$E_{tot} = E_{ex} + E_Z + E_{mc} + E_d \quad (1)$$

- The exchange energy term  $E_{ex} \propto (\nabla \cdot \mathbf{M})^2$  is at the origin of ferromagnetic ordering. It favours the parallel alignment between the magnetic moments as discussed before.
- The Zeeman energy  $E_z = -\mu_0 \mathbf{H}_{ext} \cdot \mathbf{M}$  corresponds to the interaction between the magnetization and an external field which tends to favour parallel alignment of the magnetic moment with the external field.
- The magneto-crystalline energy  $E_{mc}$  takes its origin from the spin orbit coupling meaning the interaction between the spin of an electron and its orbital motion in a crystalline structure. The magnetization tends to align with respect to the crystallographic easy axis of the material. Additional types of anisotropies could be taken into account such as shape anisotropy, magnetoelastic anisotropy, etc...
- The dipolar energy  $E_d = -\frac{1}{2} \mu_0 \mathbf{H}_d \cdot \mathbf{M}$  refers to the interaction between the magnetic moments and a demagnetization field  $\mathbf{H}_d$  created internally.

### 2.1.2 Landau-Lifschitz-Gilbert equation

The magnetization dynamics of a classical macro-spin  $\mathbf{M}$  in an effective magnetic field  $\mathbf{H}_{eff}$  is described by the Landau-Lifschitz-Gilbert (LLG) equation:

$$\frac{d\mathbf{M}}{dt} = \gamma \mu_0 \mathbf{H}_{eff} \times \mathbf{M} + \alpha \mathbf{M} \times \frac{d\mathbf{M}}{dt}, \quad (2)$$

where  $\gamma = g\mu_B/\hbar$  is the gyromagnetic factor,  $g$  the Landé factor,  $\mu_B = e\hbar/2m_e$  the Bohr magneton and  $\alpha$  the Gilbert damping constant. Gilbert damping has been first introduced in the LLG equation in a phenomenological way. It is related with a non-linear relaxation phenomenon and it controls the rate at which the magnetization reaches equilibrium.  $\mathbf{H}_{eff}$ , the effective field seen by the magnetization, is the functional derivative of the magnetic energy density  $E_{tot}$  with respect to the magnetization. Contributions

from all terms of eq (1) have in principle to be taken into account. However, the largest contribution to the effective magnetic field is provided by the demagnetization field and will solely be considered in the following.

### 2.1.3 Ferromagnetic resonance

As stated by eq. (2), the magnetization precesses around the axis given by  $\mathbf{H}_{eff}$ . When an oscillating in time magnetic field is applied in a transverse direction of the magnetization at the correct frequency (given by  $\gamma\mu_0 H_{eff}/2\pi$ ), the ferromagnetic resonance can occur. Thus, for a given frequency set by the external magnetic field, the coupling between an external electromagnetic field and the magnetic moment of a ferromagnetic material can be resonant. The resonant absorption of the power of the electromagnetic field by the magnetic moment triggers the precession of the magnetization around its equilibrium position. This phenomenon is called ferromagnetic resonance (FMR). In the relevant limit of an infinite plate for a ferromagnet with small coercivity as in our case, the resonance condition, known as the Kittel Formula, is given by :

$$f_{res} = \frac{\gamma\mu_0}{2\pi} \sqrt{H_{ext}(H_{ext} + 4\pi H_S)} \quad (3)$$

with  $\mu_0$  the vacuum permeability,  $M_S$  the saturation magnetization and  $H_{ext}$  the external applied magnetic field.

## 2.2 Spintronics of FM/NM bilayers

The most common way to inject spin polarised current is the use of the interface between a ferromagnetic material (FM) and a non magnetic material (NM). As discussed before, there is an unbalance between the density of states of spin up and spin down electrons in the ferromagnetic material which is not the case in non magnetic materials. In a model where two independent channels are considered for spin up and spin down, this induces a difference of conductivity for these two channels. A charge current passing through a ferromagnetic material is thus spin polarised. As a consequence, at the interface FM/NM, the spin polarised current is responsible for a spin unbalance in the NM layer leading to the propagation of spin current perpendicular to the interface. This spin unbalance in the NM layer will decay in the NM over a characteristic distance called spin diffusion length  $\lambda_s$ . However, this method suffers from the significant difference of conductivity between the FM and the NM layers which decreases the injection efficiency.

## 2.3 Spin pumping

During my internship, I have work on developing a different method of spin injection called spin pumping which circumvents this conductivity mismatch issues.

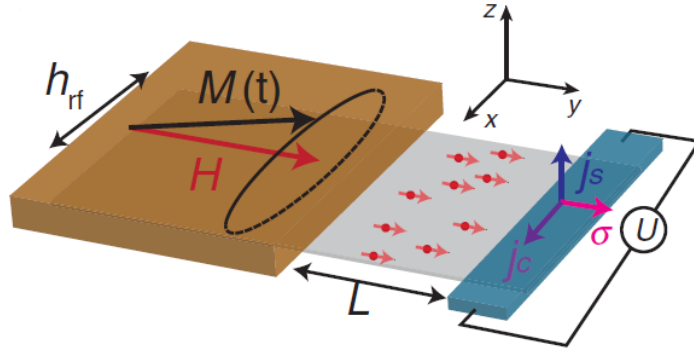


**Figure 2.2:** Spin pumping experiment principle with the ferromagnetic material (brown) pumping a pure spin current in a non magnetic material (grey) being graphene. The detection is done via Inverse Spin Hall Effect (blue contact). Extracted from [18].

It consists in driving the magnetization of a ferromagnet to resonance under the application of an RF magnetic field. It provokes the precession of the magnetization around its equilibrium position (fixed by the externally applied magnetic field). The resonant excitation of the ferromagnetic material injects spin angular momentum through the interface between the FM layer and the NM layer creating an imbalance of spin population in the NM material: the FMR can be seen as a peristaltic pump for spins. This extra spin pumping in the NM has thus an impact on the magnetization dynamic because it adds an additional component to the Gilbert damping term. It is the equivalent to adding a relaxation channel in the FM resulting in the decrease of amplitude of the magnetization precession. The efficiency of the spin injection is given by the effective spin mixing conductance, which can be extracted from experimental data with:

$$g_{\uparrow\downarrow} = \frac{M_S d_{FM}}{\hbar f} (\Delta_{H,FM/NM} - \Delta_{H,FM}) \quad (4)$$

with  $d_{FM}$  the thickness of the ferromagnetic layer,  $\Delta_{H,FM/NM}$  and  $\Delta_{H,FM}$  being respectively the line-width of the FMR of a FM/NM hetero-structure and of a sample without NM layer. So in principle measuring the extra dissipation due to the spin pumping in the normal material can give access to this crucial parameter: the more extra dissipation is induced the more spin have been injected in the non magnetic material. The experimental determination of this parameter is also crucial as it can be compared to theoretical predictions based on Landauer-Buttiker scattering approach of the FM/NM interface [16, 17].

## 2.4 Inverse spin Hall effect

A pumped spin current propagating in a non magnetic material is composed of two components: a constant component in the direction of the magnetization (DC current) and a microwave component in the perpendicular plane rotating at the frequency of the exciting microwave field (AC current). The AC current, while being one order of magnitude more intense, is more difficult to detect such that in the following we have first focused in detecting only the DC part of the spin current. The method chosen will be by exploiting the inverse spin Hall effect.

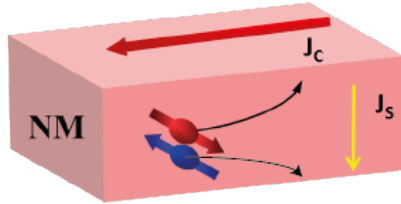


**Figure 2.3:** Schematics of the charge current and spin current conversion with the Spin Hall Effect as the spin-orbit coupling deflects electrons depending on their spin orientation.

Spin Hall effect (SHE) and its reciprocal the inverse spin Hall effect (ISHE) allow efficient charge to spin conversion. To understand it, let's recall briefly what is the usual Hall effect first. The standard Hall effect is known as the appearance of a transverse tension when charge carriers propagate in the presence of a perpendicular magnetic field. Due to the Lorentz force, charge carriers are deflected on one side or the other of the bar, depending on the relative sign of their charge. The spin Hall effect (SHE) refers to a similar segregation of carriers but in this case it is depending on their spins orientation. As sketched in figure 2.3, even without externally applied magnetic field, the spin-orbit coupling (SOC) induces, for a charge current  $j_c$ , a segregation of carriers on each side of the metallic bar, depending on their spin direction, *i.e.*, a transverse pure spin current  $j_s$ . Thus, reciprocally, with the ISHE, a pure spin current can lead to a charge segregation on the side of the bar, *i.e.* a measurable electromotive force with appears as a voltage across the SOC bar. Experimentally, the spin-orbit coupling being proportional to  $Z^4$ , where  $Z$  is the atomic proton number, materials with strong SOC are materials containing heavy elements such as Pt, Pd, etc. However, how to design efficient spin injection and detection with a SOC bar is a very challenging task as it relies on finding the good compromise for the bar metal and thickness  $l$ . Two antagonistic effects are at work. For an efficient spin-to-charge conversion one need  $l$  bigger than the spin-orbit length  $l_{so}$  while  $l$  needs to be small compared to the spin diffusion length for the spin direction not to be randomized before being detected when reaching the bar sides. In our case, we have

chosen a Palladium bar of a thickness of 8 nm, as such thickness has allowed successful previous experiments of spin injection and detection.

# My work

My supervisor François Mallet has joined the MPQ laboratory last September. His plans here are to take benefits from his expertise in microwave engineering to investigate pure spin transport in 2D van der Waals hetero-structures. As a first experiment, it has been decided to try to reproduce a recent experiment, made in Christian Schönenberger group recently, where pure spin currents have been injected in graphene through FMR based spin pumping and detected through the ISHE [18]. I have been in charge of settling this completely new experiment from scratch. I will present here my work on designing the devices and developing their nanofabrication. Finally, preliminary data of FMR on Cobalt thin films will be presented at the end of this report.

## 3.1 Simulations

I began my work with simulations of the RF antenna handled on the software COMSOL. It is a software based on advanced numerical methods of finite element calculations which allows to model and study almost realistic microwaves circuits. Indeed analytical formula are absent (or too heavy) to predict devices with complex geometries (with potential impedance mismatch) or when, for instance, ohmic or microwave losses have to be taken into account. This is a necessary step for a better understanding of our devices and their future optimizations. Yet, this part of my internship was a big challenge since this software had never been used before by any members of the group to simulate microwave fields. Therefore, I had to begin from scratch to master the basics of this software. I have begun the simulation with a simple microstrip in 2D then in 3D. The microstrip is simply two metallic layers of a given thickness and width sandwiching a dielectric substrate. As depicted in figure 3.1, the first step was to design the microstrip with the desired geometry and dimensions. It is then placed on top of a thin box representing the substrate. The overall structure is drawn inside a larger box representing the environment of the microstrip which is air (taken as vacuum). To compare with well known formula, we have first made the microstrip and the bottom plane of the substrate as Gold and the dielectric substrate as pure Si. Two lumped ports are positioned at the two extremities

of the microstrip for the propagation of the electromagnetic wave. Finally, we needed to impose scattering boundary conditions to the box representing air. It is a boundary to the outside world which is transparent to outgoing wave to mimic the infinite extension of the environment around the microstrip.

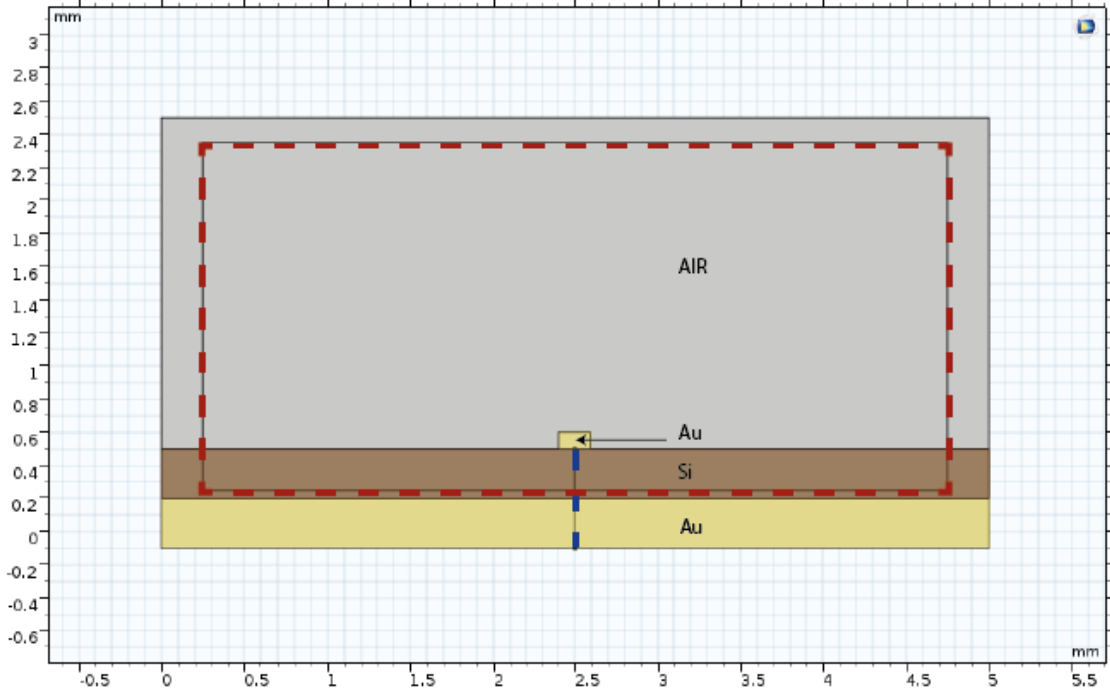


**Figure 3.1:** Geometry of the 2D microstrip designed on COMSOL. A  $190 \mu\text{m}$  wide and  $100 \mu\text{m}$  thick gold strip is placed on a  $300 \mu\text{m}$  thick Si substrate of relative permittivity  $\epsilon_r = 11.7$  backed with another gold layer. The red (resp. blue) dashed line represents the integration path for the magnetic (resp. electric) field to numerically evaluate the characteristic impedance of this transmission line.

A simulation of the typical cross-section on the magnetic field at 1 GHz has been done and is presented in figure 3.2. One recognizes the typical field lines of an "Oersted"-like field with the magnetic field circling around the central conductor. The same simulation for the distribution of the electric field is reported in figure 3.3, where one recognizes mainly the field line of a plate capacitor formed by the microstrip top conductor line and the ground plane below the silicon substrate. These simulations are still ongoing but are already a good support for the fabrication of the RF antenna. For instance, even for more complex geometries, it will allow us to find the region where we should get the maximum of the magnetic field, which is highly desirable to maximize the spin pumping mechanism. Obviously, here it indicates clearly that we need to put our devices as close as possible to the microstrip line in order to optimize the excitation of the ferromagnet. This illustrates our choice to place the device on top of the microwave line. As it will be presented in the nanofabrication part, this comes at a cost of a complexification of the nanofabrication process, as the 2D van der Waals hetero-structures will have to be

electrically isolated from the RF antenna. This will be done by using hBN flakes.

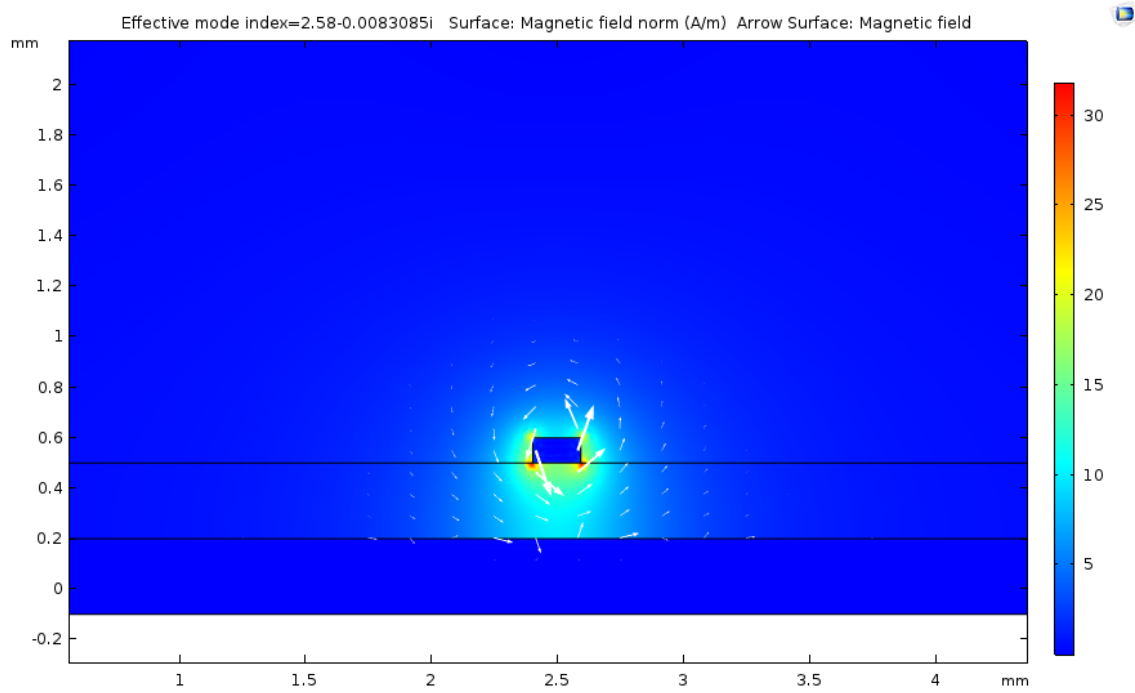


**Figure 3.2:** Magnetic field of a 2D microstrip simulated by COMSOL at 1 GHz.

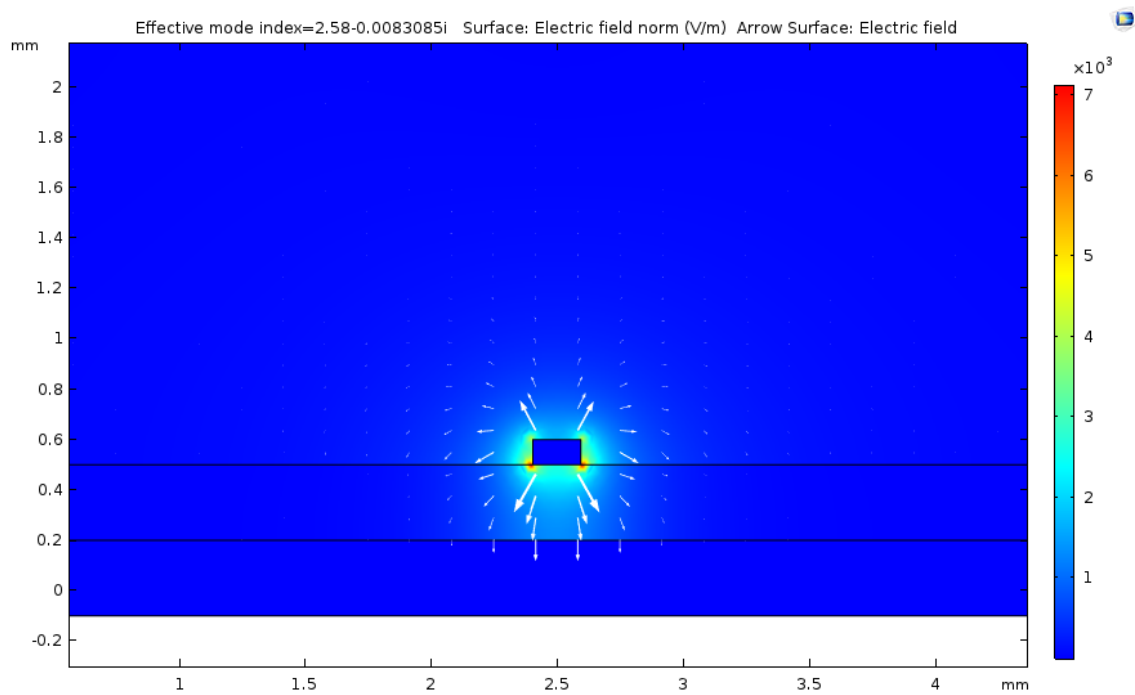


**Figure 3.3:** Electric field of a 2D microstrip simulated by COMSOL at 1 GHz.

From these simulations of the electric and magnetic fields, we have also been able to implement a numerical method to evaluate the impedance  $Z = V/I$  of any microwave lines.

The control on this quantity is very important. As good as possible impedance matching between the circuit, the measurement lines and the RF apparatuses is mandatory at microwave frequencies to minimize reflection and thus maximize the microwave power available on the sample at the ferromagnet position.

Indeed, as  $\mathbf{E} = -\mathbf{grad}V$  we can get from the electric field simulations  $V$  with,

$$V = - \int_L \mathbf{E} \cdot d\mathbf{l} \quad (1)$$

where  $L$  is the path represented in the figure 3.1 by the blue vertical dotted line. And from Ampère theorem, we can get the current  $I$  as:

$$I = \frac{1}{\mu_0} \oint_C \mathbf{B} \cdot d\mathbf{l} \quad (2)$$

with  $C$  being the closed path represented in the figure 3.1 by the red dotted rectangle.

The impedance of this standard microstrip obtained by this method with COMSOL is equal to  $49.64 (-0.16i) \Omega$  (the negligible imaginary part is not completely understood but is interpreted as coming from small microwave losses due to numerical effects or from the finite integration paths and the open boundary conditions), in excellent agreement with the analytical formula giving also  $50 \Omega$  (see figure 3.4 for comparison). This is an achievement to have been able to obtain from COMSOL such an agreement on this simple model. It validates our ability to use COMSOL to simulate and study much more complex circuits accurately. However, there is still ongoing work to do so. Other parameters must be taken into account in the model such as the doping of the substrate which influences its conductivity and its microwave losses, the thickness of the  $\text{SiO}_2$  capping of the substrate and its permittivity which differs from bulk Si... Also, the study a 3d microstrip is in progress but requires more work to make a good compromise between the density of the mesh which is linked to the accuracy of the calculations and the computation time. If the simulations and calculations done in COMSOL for a given type of geometry are expected to be more accurate and faithful to the reality, to design quickly our first RF circuits we have relied on the software TX-LINE to calculate rapidly the impedance and the geometry parameters of the RF antenna. But as it is based only on an analytic formula for simple geometries (only one dielectric and infinite ground plane for instance can be considered), it results in poor flexibility and accuracy when it comes to real RF circuits compared to COMSOL results. Therefore, the future design our RF antenna will only be based on COMSOL simulations.

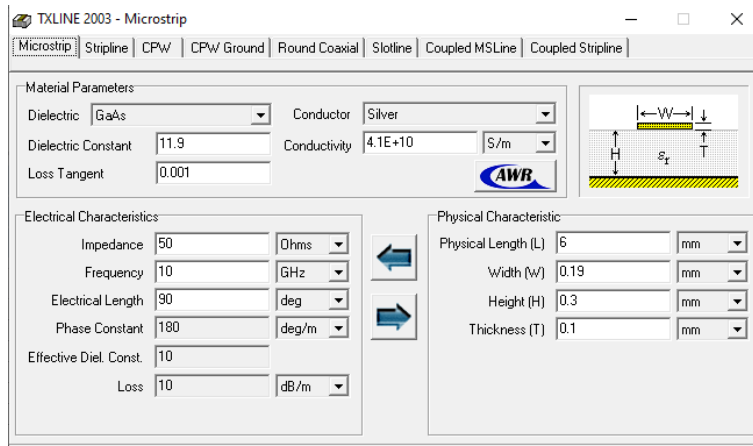


**Figure 3.4:** Computation of the impedance and dimension of the RF antenna through TX-LINE

## 3.2 Optical masks

In parallel to the simulations, I have also been in charge of the design of optical masks for the realization of the RF antenna and the contacts for the DC current measurements. The masks were done through the platform Pioneer Two. I have reproduced different types of geometry for the RF antenna to explore their performances. Beside the microstrip line previously discussed, another commonly used microwave transmission line is the coplanar waveguide (CPW), which is formed from a conductor between a pair of ground planes, on top of a dielectric medium. The ratio of the gap between the ground and conductor planes and the width of the central strip allows to tune the characteristic impedance. These parameters had to be adapted from the geometry of the CPW of the printed circuit board (PCB) associated with a conductor plane width of  $380 \mu\text{m}$ . The thickness of  $300 \mu\text{m}$  of the dielectric substrate is also fixed according to the wafers available in the clean-room. In our case, the substrate is made of  $\text{SiO}_2$  (with a thickness of  $280 \text{ nm}$ ) on top of doped Si. The CPW has been designed by progressively decreasing the conductor width from  $400 \mu\text{m}$  to  $10 \mu\text{m}$  and adapting the gap value in order to keep a constant impedance of  $50 \Omega$ . How one has to reduce the gap as a function and the central conductor width to remain  $50 \Omega$  matched has been handled using the software TX-LINE.

The other RF antenna geometry investigated is, as already mentioned, the microstrip. Here, there is only one conductor plane and the crucial parameters for satisfying the impedance requirement are only its width and the thickness and dielectric constant of the substrate. I have designed the strip-line in a way that the line width is  $50 \Omega$  matched (even with bends) over a distance as long as possible. This transmission line is reduced progressively only in the middle where the samples will be positioned. While this design is clearly not  $50 \Omega$  matched where the spintronics devices will be placed, nevertheless its symmetry ensures a magnetic field maximum at this specific location.

In addition, I have drawn two more masks taking the two previous masks and rotating them by  $90^\circ$  in order to study the effects of having a magnetic field perpendicular to the axis of the antenna. The four types of antennas have been grouped in one drawing. This file has been sent to a company which has built the final optical mask. The optical mask is a squared piece of glass into which the design has been printed with chrome.

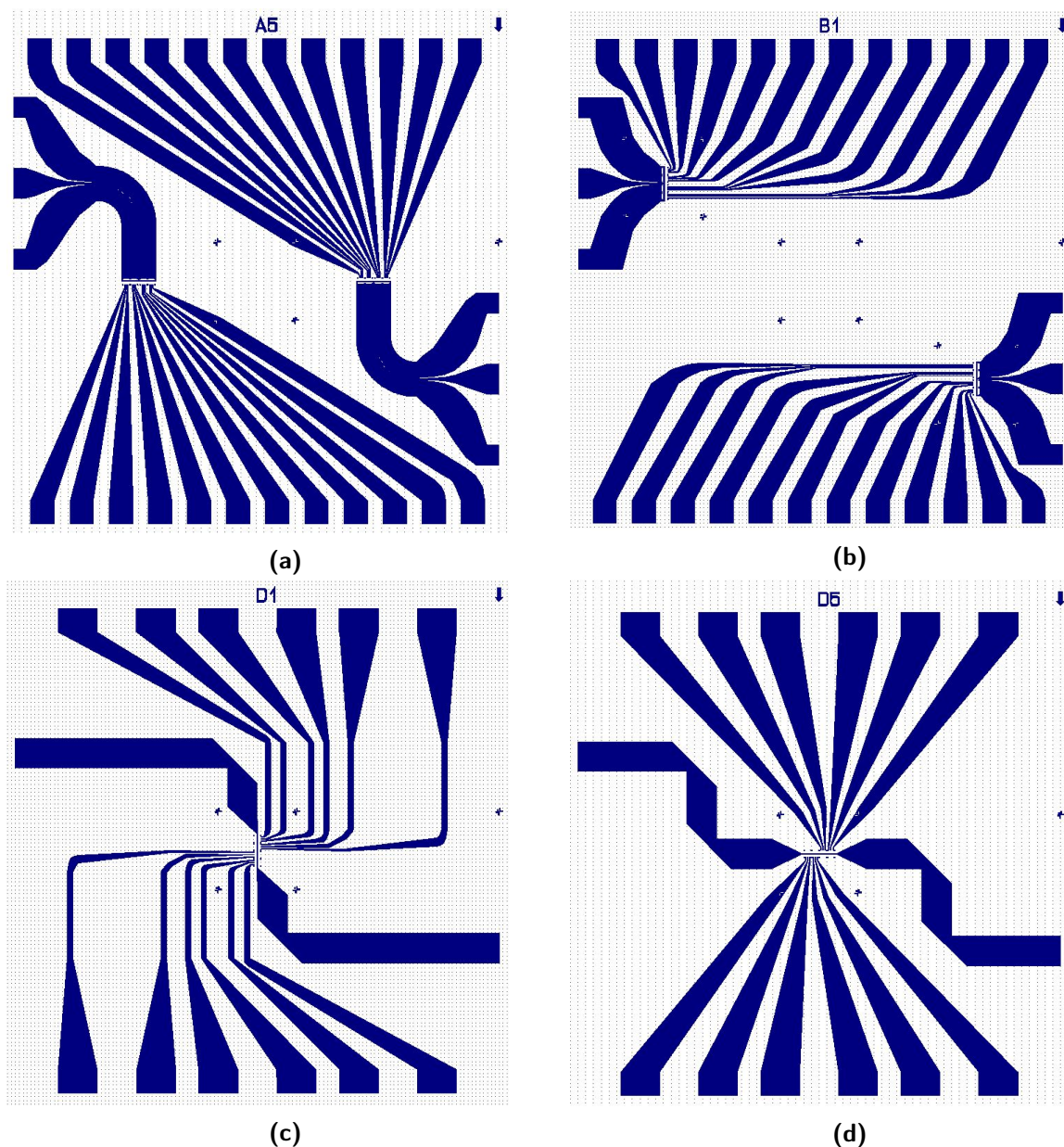


**Figure 3.5:** Design of the optical masks for different types of RF antenna: the CPW (a) and the microstrip (c) with their respective geometry rotated by  $90^\circ$  (b and d).

Finally, many lines that are all directed to the RF excitation zone can be observed on our masks. As presented previously, the method chosen to detect its propagation in the graphene is the measure of the electromotive force across the Pd contact induced by ISHE. However, signal of a few tens of nV are expected for spin pumping over several

$\mu\text{m}^2$  FM/NM interface, These many lines allows to have multiple voltage probes on the several devices (see figure 3.8) which have been put in series to collect a bigger voltage.

### 3.3 Nanofabrication

The fabrication of the samples required different steps I have been trained to in the clean-room. The samples were fabricated on a 300  $\mu\text{m}$  thick wafer doped Si with a 280 nm thick of  $\text{SiO}_2$ .

The first step is the photolithography using the optical masks I have designed. One must use a photoresist sensitive to UV light to transfer a pattern. In particular, I have used the AZ5214E, a positive photoresist which can also be reversed into a negative resist. The interest is that after the development step, the overall result is a negative wall profile of the photoresist ideally suited for lift-off. Finally, the fabrication of the antenna and the DC contacts ends with a deposition by evaporation of layers of Ti (5 nm) and Au (100 nm) followed by the lift-off process.

Then, I have proceeded a transfer method called "hot-pickup" to build heterostructures of hBN and graphene on top of the RF antenna. A key feature of this technique is the rapid batch fabrication of many heterostructures. This technique consists of using a glass slide on which is deposited a drop of Polydiméthylsiloxane (PDMS) coated with Polypropylene carbonate (PPC). This drop is used to catch (pick-up) or release (drop-down) materials by varying the temperature below or above the glass transition temperature of the PPC respectively. Two wafers of exfoliated graphene and exfoliated hBN, as well as the sample fabricated from the last step, are positioned into a hot plate located into a micro-manipulator basal plane. The drop of PDMS/PPC is mounted on a micro manipulator arm to be able to move it in the plane and in the z direction. An optical microscope is used to perform the pick-up and drop-down by precisely aligning the drop with the desired flake of material or the target wafer. The process is shown in the figure 3.6 and the pick-up station located in the clean room is represented in figure 3.7. The pick-up was realised around  $75^\circ\text{C}$  by making in contact the drop and the flake of material. After, the drop was removed slowly. The drop-down is done at  $84^\circ\text{C}$  and above. In particular, the drop-down at this temperature is completely melting the drop such that the tip of the drop is left on the wafer after the drop removal. This is done because of the poor adhesion of hBN with the gold antenna. The PDMS/PPC left on the wafer is then cleaned in a solution of acetone followed by a cleaning in isopropanol. The goal is to cover the entire antenna to maximize the number of device. The flakes are selected such that they are as large as possible and also very thin. A compromise between the thickness and the size had to be done because of big issues for the exfoliation and pick-up of monolayers. Therefore, I have been able to pick-up hBN flakes with thickness

around 20 nm and tens of nanometer thick graphene flakes with a sufficient size fitting with the width of the antenna.

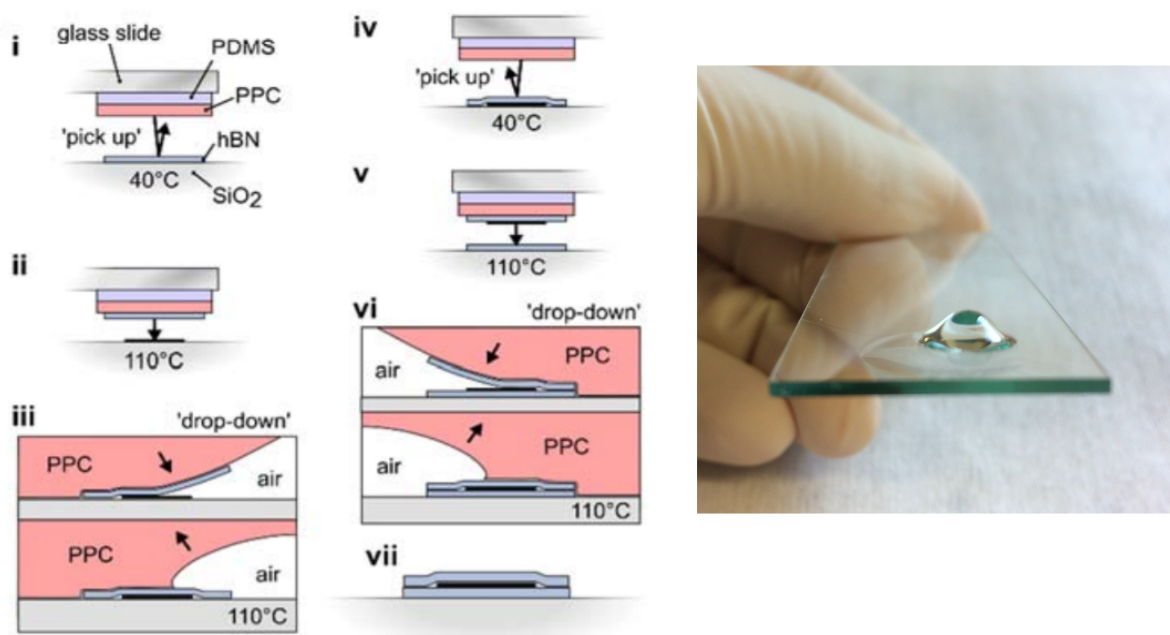


**Figure 3.6:** (left) Schematic of the hot pick-up method. In this example, a layer of hBN and a layer of a given material are transferred to form an heterostructure of this material sandwiched between two hBN layers. Extracted from [19]. (Right) Typical PDMS/PCC drop used in our group for the hot pick-up.

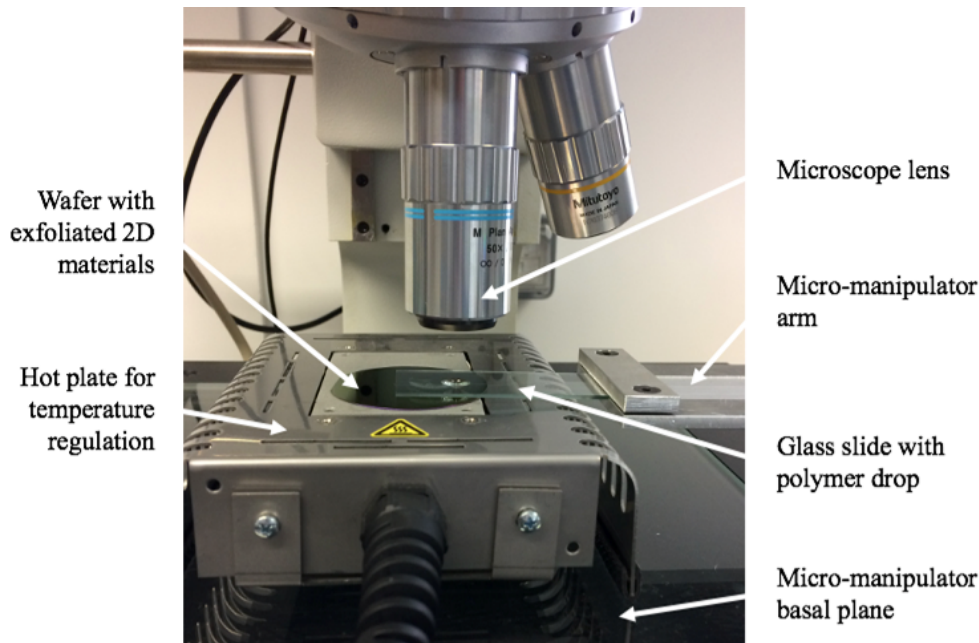


**Figure 3.7:** The TELEM pick-up station. A micro-manipulator allows to transfer van der Waals layers from a wafer with exfoliated 2D materials to the device wafer. The temperature of the wafers is tuned with the hot plate and a microscope allows displacement accuracy at the micrometer range.

In the following, 4 steps of electronic lithography are required. A positive resist is used called Polymethyl methacrylate (PMMA) which is sensitive to electrons. After, each electronic lithography, the development of the resist is necessary to remove the regions of the resist exposed by the electron beam. The deposition technique is the evaporation. The pressure of the evaporator chamber is lowered below  $10^{-6}$  mbar. The sample holder is rotated and a sufficiently low deposition rate is chosen to ensure a clean and homogeneous deposition. Only after the deposition step, a lift-off in acetone is made to remove the material in the regions where it is superposed over resist.

- The first electronic lithography is performed in order to etch graphene and limits its dimension into an  $8 \times 5 \mu\text{m}^2$  rectangle. The reactive ion etching (RIE) method is employed. It uses oxygen to selectively etch graphene.
- The second electronic lithography aims to build the cobalt  $4 \times 4 \mu\text{m}^2$  contact right on top of graphene. The cobalt layer of thickness 50 nm and a capping of 5 nm thick gold are deposited through evaporation.
- The third step allows to form the contact of palladium for the detection of the voltage induced by ISHE. The deposition of a 8 nm thick Pd layer is proceeded through evaporation as well.

- The final electronic lithography is needed to pattern smaller Ti/Au contacts to connect the contacts created during the photolithography and the Pd contacts. 2 nm of Ti and 60 nm of Au are deposited.

Pictures of the typical fabricated device is shown in the figure 3.8 and figure 3.9.

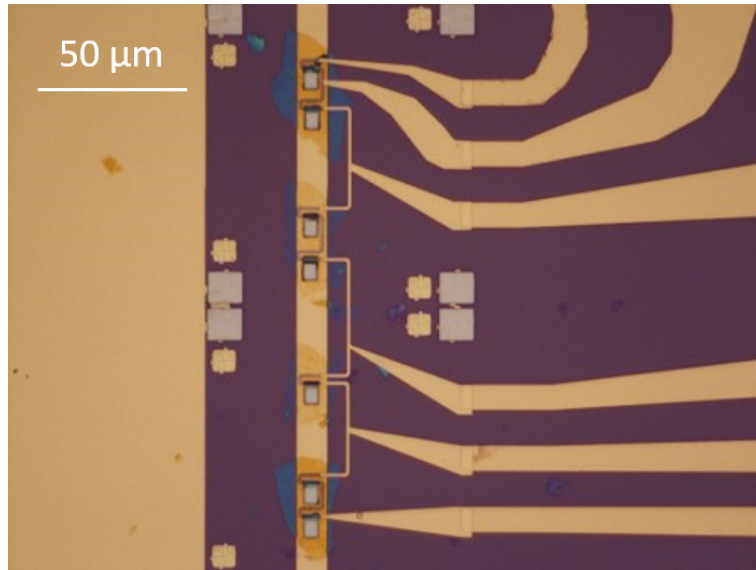


**Figure 3.8:** Image of the sample taken on an optical microscope. The device for spin pumping is composed of a contact of Co (light grey squares) for the spin injection and Pd for the detection deposited on a layer of graphene. A certain number of device fabricated in series are on top of a Ti/Au CPW which is isolated with hBN (blue flakes). On the right, big Ti/Au contacts are used for the detection part and connect the sample to the measure instruments.

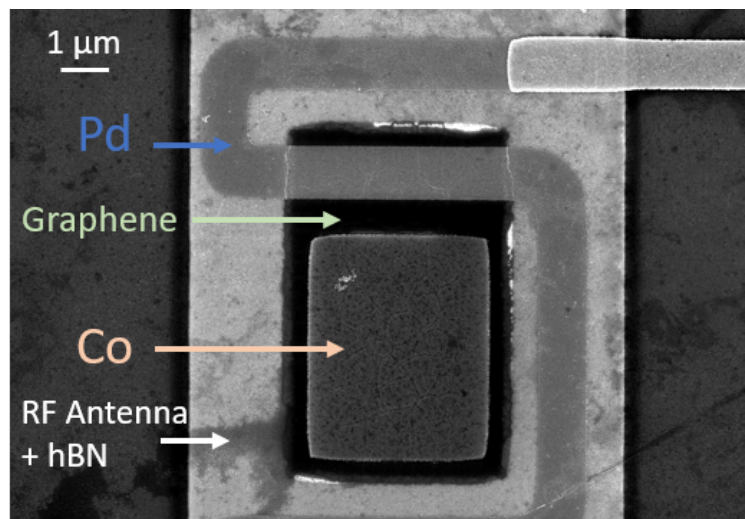


**Figure 3.9:** Image of the sample taken on a Scanning Electron Microscope (SEM). A thin graphene layer is deposited on the RF antenna which is isolated by a layer of hBN. The Co and Pd contacts are built on top of graphene for the injection and detection of the spin current in graphene respectively.

I have made multiple trials to correctly fabricate the samples. I had different issues along the fabrication process which i corrected progressively. First, i encountered a difficulty when arriving to the step of the Co lift-off. When the sample was immersed into the acetone bath, after a few hours, the heterostructure of hBN/Graphene/Co was coming off of the gold RF antenna. I supposed that it was because of the weak interaction between hBN and gold, and also because the hBN flakes were too close together and sometimes superposed to each other. Therefore, when one flake was not well attached to the antenna, the flakes were collectively lifted off. For the future samples, i decided to deposit on the antenna well separated hBN flakes. Another issue concerned the Pd electrode for the detection part. At first, i have made the meander of Pd not completely on the RF antenna. There were parts of it going down and up the 100 nm step of the gold antenna. As the Pd thickness is only 8 nm, the Pd meander was not continuous everywhere. To overcome this issue, the Pd meander has been only deposited on top of the RF antenna and contact of Ti/Au were added to connect the Pd and the big Ti/Au contacts made by optical lithography. Finally, we realised that the graphene/Co/Pd heterostructure needed to be perfectly isolated from the antenna by hBN, which required perfect alignment during the lithography step. Finally, all these remarks led us to the sample shown in 3.8.

### 3.4 Measurements

Finally, the sample is placed on the sample holder. Ultrasonic micro-wire bonding is performed to connect the sample (antenna and DC contacts) to the microwave printed circuit board (see figure 3.10 right). The sample holder is then mounted between two coils which produces a magnetic field fixing the magnetization of the ferromagnetic material along their axes (see figure 3.10 left). The RF excitation is generated by a microwave source allowing the control of the applied frequency and power. The microwave power flowing out of the device is measured with a spectrum analyzer locked at the microwave source frequency. All control and measurement instruments are all interfaced in python and controlled with a generic interface on a computer. Two types of measurement are possible, depending on the type of the chosen RF antenna. The CPW geometry requires reflection measurements which can be perform using a board band directional coupler. In this case, only one port for output and input signal is required. As the PCB has two ports, it is possible to do measurements on two devices one after the other. For the microstrip, the measurements are done in transmission. Therefore it requires the two ports, one for the input and the other for the output signal. As presented previously, the study of the microwave absorption allows to detect the FMR and the injection of spin currents in graphene and the method chosen to detect its propagation in the graphene



**Figure 3.10:** Experimental setup. Left: the sample holder, attached on a motorized rotation axis, is centered in the middle of the Helmholtz coils magnet. Green microwave cables connect it to the microwave generator and spectrum analyzer. Right: zoom on the PCB where CPW lines can be seen connecting the microwave cable to the on chip device.

is the measure of a voltage across the Pd contact induced by ISHE. However, signal of a few tens of nV are expected, such that, several devices (see figure 3.8) have been put in series to collect a bigger voltage due to ISHE.

Control measurements have been done on a simpler sample than the one mentioned in the section Nanofabrication. The sample is formed by a  $\text{SiO}_2$ /doped Si wafer coated with a 50 nm thick Co layer and a 5 nm thick Au capping layer positioned directly on top of a microstrip transmission line. The transmitted power  $P$  through the microwave line, for an approximately 0 dBm microwave power at the wafer position, as a function of the externally applied magnetic field  $H_{ext}$  has been measured for different frequency  $F$  of the exciting microwave field. Data taken at  $F$  of 6.8 GHz sweeping up (resp. down) the externally applied magnetic field are presented in figure 3.11 (resp. 3.12). Beside a similar magnetic field "V-shape" background, two specific features can be observed. A more pronounced deep appears only at a positive field when coming from large negative fields (see fig. 3.11) and reciprocally only at a negative field when coming from large positive fields (see fig. 3.12). Such hysterical behavior is reminiscent of the magnetization reversal when external magnetic field exceeds the coercive field  $H_c$  as depicted in the figure 2.1. It is therefore attributed to this phenomenon.

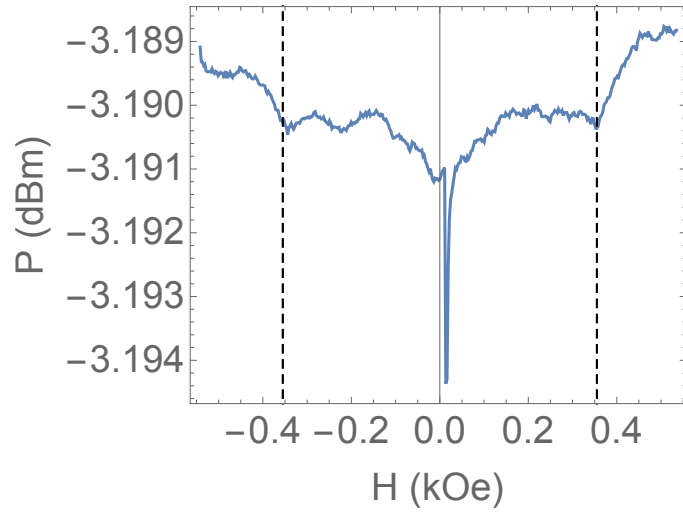


**Figure 3.11:** Typical transmission power spectrum taken at  $F = 6.8$  GHz as a function of the applied magnetic field ramping up. Two specific features can be observed. Spotted by the dashed, two deeps can be seen at a specific magnetic field (both positive and negative) which depends on the microwave excitation frequency (see color density plot of 3.13). They are attributed to the excitation of the FMR of the Cobalt film. A more important deep is observed at +16 Oe approx which is frequency independent (see figure 3.13).

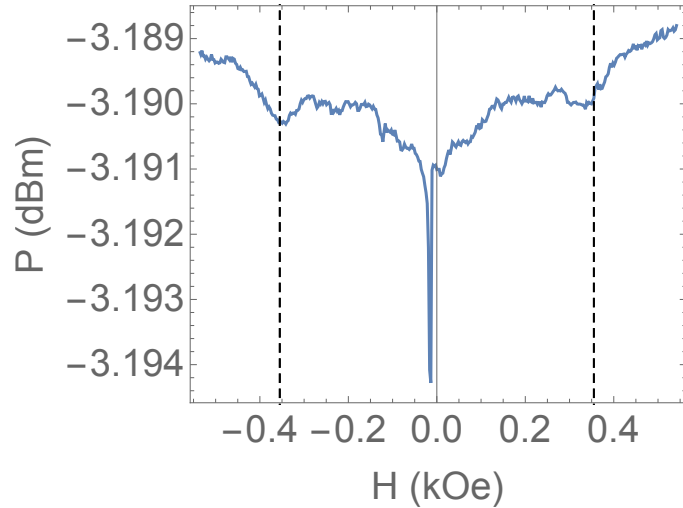


**Figure 3.12:** Same data as in 3.11 but with ramping down the magnetic field. The FMR deeps (dashed line) are unchanged while the more important frequency independent deep is now observed at -16 Oe.

Similar microwave power spectra has been measured for different excitation frequency ranging from 8 GHz to 5 GHz. Such data are presented in the colored density plot of figure 3.13 where the transmission has been average for both external magnetic field ramping up and down. The mean transmission for each frequency has also been subtracted to remove the frequency dependent back ground of the setup. The absorption deeps attributed to the magnetization reversal are indeed frequency independent, confirming our hypothesis.

On the contrary, the positions of the two symmetric in magnetic field deeps evolve with the excitation frequency. The fit of their characteristic magnetic field as a function of the excitation frequency with the Kittel equation given in (3) is represented by the black dashed line, with the parameters set to  $\frac{\gamma\mu_0}{2\pi} = 3.2$  GHz/kOe and  $4\pi M_S = 13$  kOe. These values are in complete agreement with what can be found in the literature for similar Cobalt film thickness and thus validate the experimental setup [20]. However, as seen in the data of 3.11 and 3.12, the amount of microwave power absorbed by the FMR appears pretty small, below 1 mdBm. It thus implies long acquisition time to be resolved, typically 10 hours for the spectrum presented in 3.13, which means we are highly sensitive to low frequency electronic noise and temperature drifts in the laboratory.

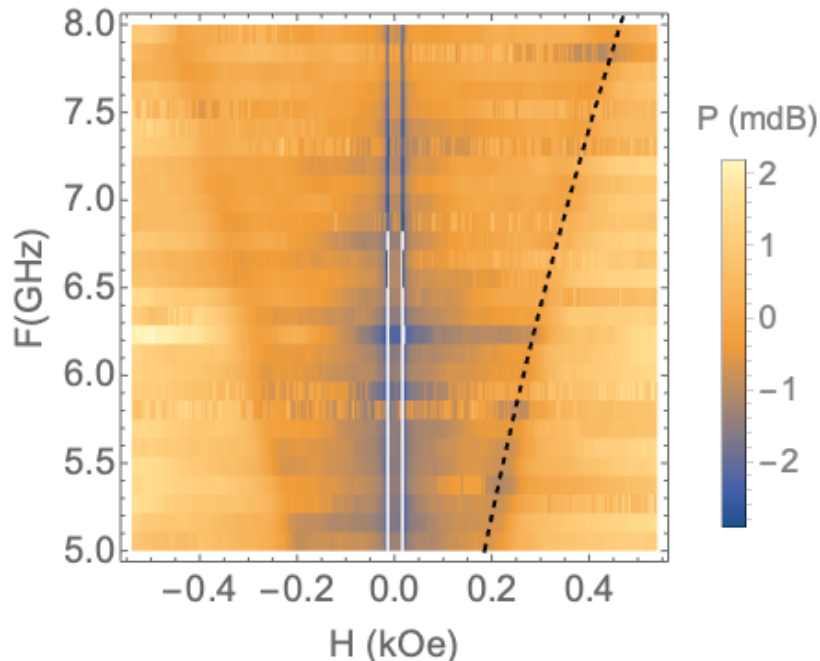


**Figure 3.13:** FMR of a cobalt thin film. The mean transmitted power at each microwave excitation frequency has been subtracted to remove the frequency depend transmission background of the experimental setup which would hide the FMR deep. The dashed line is a fit of the data to the Kittel equation with the parameter given in the main text.

Last week, I have tried to combine this FMR measurement with the voltage measurement at the Pd electrode terminals in the complete sample presented in the nanofabrication part of this report. Unfortunately, no significant signal has been observed, probably due to the already mentioned low frequency noise. Two lock-in detection schemes will be implemented to circumvent this issue, one where the external magnetic field is modulated at a few tens of Hz and another one where the frequency of the microwave excitation will be modulated at a few tens of MHz.

# Conclusion

This internship is about a totally new experience which my supervisor François Mallet, who joined the laboratory last September, is currently settling up. Building a new experiment from scratch is always challenging, but extremely formative. I have performed many various tasks, from microwave design and simulation to a lot of clean-room fabrications. I have also participated to the finalization of the experimental setup. This last part has not been reported here but it has consisted in some soldering, installing measurement apparatuses, interfacing them... At this point of this internship, even if we did not manage to finalize the planned experiment, I believe that the main necessary bases have been laid and that by improving our detection schemes we are close within a couple of months to be able to observe spin pumping effect in our devices.

# Bibliography

- [1] J. Bardeen and W. H. Brattain, "The Transistor, A Semi-Conductor Triode", *Phys. Rev.* **74**, 230 (1948)
- [2] E. Mollick, "Establishing Moore's Law," in *IEEE Annals of the History of Computing*, vol. **28**, no. 3, pp. 62-75 (2006)
- [3] S. E. Thompson, R. S. Chau, T. Ghani, K. Mistry, S. Tyagi and M. T. Bohr, "In search of "Forever", continued transistor scaling one new material at a time," in *IEEE Transactions on Semiconductor Manufacturing*, vol. **18**, no. 1, pp. 26-36, (Feb. 2005)
- [4] T. Mizuno, N. Sugiyama, A. Kurobe and S. -. Takagi, "Advanced SOI p-MOSFETs with strained-Si channel on SiGe-on-insulator substrate fabricated by SIMOX technology," in *IEEE Transactions on Electron Devices*, vol. **48**, no. 8, pp. 1612-1618, Aug. 2001
- [5] S. Sinha, G. Yeric, V. Chandra, B. Cline and Y. Cao, "Exploring sub-20nm FinFET design with Predictive Technology Models," *DAC Design Automation Conference 2012*, pp. 283-288
- [6] A. Fert, "Nobel Lecture: Origin, development, and future of spintronics", *Rev. Mod. Phys.* **80**, 1517 (2008)
- [7] P. A. Grünberg, "Nobel Lecture: From spin waves to giant magnetoresistance and beyond", *Rev. Mod. Phys.* **80**, 1531 (2008)
- [8] M. Julliere, "Tunneling between ferromagnetic films", *Physics Letters A Volume* **54**, Issue 3, Pages 225-226 (1975)
- [9] E.C. Ahn, "2D materials for spintronic devices", *npj 2D Materials and Applications* volume **4**, Article number: 17 (2020)
- [10] A. Avsar, H. Ochoa, F. Guinea, B. Ozyilmaz, B.J. van Wees, and I.J. Vera-Marun, "Colloquium: Spintronics in graphene and other two-dimensional materials" , *Rev. Mod. Phys.* **92**, 021003 (2020)

- [11] B. Dlubak, M.-B. Martin, C. Deranlot, B. Servet, S. Xavier, R. Mattana, M. Sprinkle, C. Berger, W. A. De Heer, F. Petroff, A. Anane, P. Seneor and A. Fert, "Highly efficient spin transport in epitaxial graphene on SiC", *Nature Physics* volume **8**, pages 557–561 (2012).
- [12] S. Manzeli, D. Ovchinnikov, D. Pasquier, O. V. Yazyev, and A. S. Kis, "2D transition metal dichalcogenides", *Nature Reviews Materials* volume 2, Article number: 17033 (2017)
- [13] A. Soumyanarayanan, N. Reyren, A. Fert and C. Panagopoulos, "Emergent phenomena induced by spin–orbit coupling at surfaces and interfaces", *Nature* volume **539**, pages 509–517 (2016)
- [14] Cao, Y., Rodan-Legrain, D., Rubies-Bigorda, O. et al., "Tunable correlated states and spin-polarized phases in twisted bilayer–bilayer graphene", *Nature* **583**, 215–220 (2020)
- [15] S. Omar and B. J. van Wees, "Spin transport in high-mobility graphene on WS<sub>2</sub> substrate with electric-field tunable proximity spin-orbit interaction", *Phys. Rev. B* **97**, 045414 (2018)
- [16] Y. Tserkovnyak, A. Brataas, and G. E. W. Bauer, "Spin pumping and magnetization dynamics in metallic multilayers", *Phys. Rev. B* **66**, 224403 (2002).
- [17] Y. Tserkovnyak, A. Brataas, and G. E. W. Bauer, "Enhanced Gilbert Damping in Thin Ferromagnetic Films", *Phys. Rev. Lett.* **88**, 117601 (2002).
- [18] D. Indolese, S. Zihlmann, P. Makk, C. Jünger, K. Thodkar, and C. Schönenberger, "Wideband and On-Chip Excitation for Dynamical Spin Injection into Graphene", *Phys. Rev. Applied* **10**, 044053 (2018)
- [19] F. Pizzocchero, L. Gammelgaard, B. S. Jessen, J. M. Caridad, L. Wang, J. Hone, P. Bøggild, and T. J. Booth, "The hot pick-up technique for batch assembly of van der Waals heterostructures", *Nature Communications* volume **7**, Article number: 11894 (2016)
- [20] C. C. Tsai, J. Choi, Sunglae Cho, S. J. Lee, B. K. Sarma, C. Thompson, O. Chernyshevskyy, I. Nevirkovets, and J. B. Ketterson, "Microwave absorption measurements using a broad-band meanderline approach", *Review of Scientific Instruments* **80**, 023904 (2009)